Journal of Materials Chemistry A

ROYAL SOCIETY OF CHEMISTRY

PAPER

View Article Online
View Journal

Cite this: DOI: 10.1039/d5ta10130a

Lattice *vs.* surface water: correlation between the proton conductivity and microstructure of faujasite zeolites upon water adsorption

Glorija Medak Spahić, *[a] Marko Dunatov, [a] Jan Marčec,[b] Josip Bronić,[a] Andreas Puškarić [a] and Lidija Androš Dubraja *[a]

Zeolites are readily available crystalline materials with intrinsic porosity, and their outstanding physical and chemical properties have been demonstrated in many areas, including catalysis, adsorption, ion exchange, and gas separation. Their insulating character has so far prevented the development of zeolite-based devices; however, given their non-toxic nature and abundance, it would be worthwhile to investigate their charge transport properties, as the inherent micro-, meso- and macropores offer specific structuring and modification options for various engineering and biomedical applications. Here, two faujasite Na-FAU type zeolites with different particle sizes, nanosized (n-FAU) and microsized (μ-FAU) zeolite samples, were prepared to comprehensively investigate their electrical properties. To elucidate the complex interplay between morphology, degree of hydration, and overall electrical performance of the studied zeolites, structural (powder X-ray diffraction under ambient and non-ambient conditions), microstructural (scanning electron microscopy, light-scattering particle size analysis, and porosimetry), thermal (thermogravimetry and differential scanning calorimetry), spectroscopic (vacuum infrared spectroscopy) and electrical (impedance spectroscopy) methods were used synergistically. The research results indicate that particle size affects the ionic conductivity of zeolites (1.97×10^{-5} S cm^{-1} for μ-FAU compared with 3.00×10^{-7} S cm^{-1} for n-FAU under dry conditions), as continuous channels in larger zeolite particles provide more efficient charge transfer pathways. Another important factor for the electrical properties of zeolites is relative humidity, or the degree of hydration, which causes a 4 order of magnitude change in ionic conductivity (3.00×10^{-7} S cm^{-1} *versus* 2.75×10^{-3} S cm^{-1} for n-FAU under dry and humid conditions). This study demonstrates that the electrical characteristics of zeolites are highly tuneable, which may create new opportunities for the use of these porous functional materials in future sustainable applications.

Received 11th December 2025
Accepted 27th March 2026

DOI: 10.1039/d5ta10130a

rsc.li/materials-a

Introduction

Zeolites are inorganic crystalline materials most often composed of SiO_4 and AlO_4 corner-sharing tetrahedral units that create a negatively charged framework, whose charge is compensated by the presence of M^{n+} cations ($M = NH_4^+$, Na^+, K^+, Ca^{2+} *etc.*). Although the use of zeolites in petroleum refining and gas separation has become indispensable, there are numerous areas of research that can still benefit from their proven properties.[1] Recent discoveries showcased remarkable cation transport properties of zeolites as membranes for clean energy generation through salinity gradient.[2] The combination of high surface charge density and high porosity allows cations to diffuse through the structure, while a negatively charged framework prevents the passage of anions.[3] Furthermore, the choice of a M^{n+} cation has been found to strongly influence conductivity, to the extent that the material becomes an insulator once converted to the proton form.[4] Replacement with a multivalent cation reduces the conductivity of the zeolite as the concentration of counter ions is reduced.[5] Due to its charge and ionic radius, sodium is considered one of the best conductivity promoters for various types of zeolite frameworks (MFI, LTA, and FAU). In particular, the preference for cheap and abundant raw materials makes zeolites an interesting, environmentally friendly alternative also for the semiconductor industry, if conditions could be achieved under which the insulating character of zeolites could be altered. This insulating property has so far prevented this class of materials from receiving significant consideration for electronic applications.[6]

In addition to the aluminosilicate framework and M^{n+} counterions, the conductivity of zeolites is also influenced by other guest molecules that occupy the porous structure. Strong

[a]*Laboratory for the Synthesis of New Materials, Division of Materials Chemistry, Ruđer Bošković Institute, Bijenička Cesta 54, Zagreb, Croatia. E-mail: Glorija.Medak@irb.hr; Lidija.Andros@irb.hr*

[b]*Department of Inorganic Chemistry and Technology, National Institute of Chemistry, Hajdrihova 19, SI-1001 Ljubljana, Slovenia*

electrostatic gradients between the cations and the framework in zeolites make zeolites highly hygroscopic.[7] For this reason, under ambient conditions, water molecules from the air fill the channels and become an intrinsic part of the zeolite structure. Depending on the amount of structural defects such as silanol "nests" (Si–OH-rich areas) and the Si/Al ratio, some zeolite types can adsorb more than 25% of their mass and accommodate significant number of water molecules.[8–11] The complex pore systems of the zeolite frameworks and their affinity for intrinsic lattice water is an important factor in context of electrical transport. Within these microporous channels, depending on the zeolite structure and composition, water molecules are known to form short-range clusters through a network of hydrogen bonds.[12,13] For example, in a hydrated Na-FAU zeolite, diffuse reflectance infrared Fourier transform spectroscopy measurements suggested the presence of an unusual hexameric water cluster in the 12-ring window.[14] Recently, ^{1}H time-domain NMR measurements revealed the evolution of amorphous and crystalline ice at −20 °C in the mesopores of BPH zeolite nanosheets.[15] Moreover, water molecules can be anchored to the framework itself *via* hydrogen bonds with the Si–O(H)–Al bridges, *i.e.* the Brønsted acid sites.[16] Quantum mechanical methods confirmed the stabilising effect of water molecules on the neighbouring protons at Brønsted acid sites in the structures of MFI, FAU, and CHA zeolites.[17] Apart from the micropores (<2 nm), the zeolite structure may also contain subsequently created meso- (2–50 nm) or macropores (>50 nm).[18] Water molecules located in the intrinsic pores of the zeolites (appearing either in clusters or coordinated to metal centres) have defined crystallographic positions and site occupancies and are an integral part of the crystal structure; these can be referred to as crystal lattice water molecules. Additional water molecules can be adsorbed at the boundary between a solid crystal (crystallite) and its surrounding environment.[19] These surface water molecules can also form strong hydrogen bonds with the terminal OH groups of extrinsic meso- and macropores, as well as at grain boundaries.[10,20] When considering the transport properties of polycrystalline ceramics, the resistance of grain boundaries can significantly influence conductivity in solid ionic conductors.[21] Proton conduction through layers of adsorbed extrinsic water is a well-known phenomenon in materials similar to zeolites, *i.e.* porous monocrystalline oxides and ceramics, such as Y-stabilized ZrO_2, CeO_2, TiO_2 and SiO_2.[22,23] Depending on the level of hydration, this water is categorized as "ice-like" (strongly bound to the surface and highly ordered) in the first layers, and as "liquid-like" (loosely bound and disordered) built on the structured water layers further from the surface.[24–26] In materials without structured pore systems, surface (extrinsic) water is often the main charge carrier,[25] so it can be assumed that it also plays a decisive role in the electrical properties of hygroscopic materials such as zeolites.

However, the conductivity of zeolites has mostly been studied from the perspective of transport through the framework channels, that is, the intrinsic or crystal lattice water.[27] Furthermore, the electrical measurements on different zeolite single-crystals made it possible to account only for the electrical transport through the channels,[28] since the effects of the grain boundaries and surface are negligible in a single crystal. An interesting trend was observed, which is in contrast to the known behaviour that increasing humidity leads to an increase in proton conductivity as observed in many metal–organic frameworks and related systems.[29–31] In the zeolite pores, at higher water contents, the mobility of the ions is reduced due to the clogged channels.[28,32] These observations led to the conclusion that, in addition to conductivity driven by proton hopping through the Grotthuss mechanism, the diffusion of M^{n+} cations *via* the vehicular mechanism also contributes to the overall bulk conductivity.[22–24] In comparison to single crystals, where the transport properties of the material are bulk dominated, the contributions of the surface and grain boundaries must be considered when particle size is reduced (*e.g.* in polycrystalline samples). The role of crystal size in the conductivity of zeolites has been largely overlooked, making it difficult to determine whether the observed behaviour is a property of the bulk material or results from interactions at the surface and grain boundaries, which is important for establishing the electrical properties of the material.[6,33]

In order to better understand the effect of bulk *versus* surface contributions on the electrical properties, two faujasite Na-FAU type zeolites with different particle sizes, nanosized (n-FAU) and microsized (μ-FAU) samples, were prepared. The chemical composition, structural features, and morphological versatility of these zeolites were characterized by atomic absorption spectrometry, powder X-ray diffraction under ambient and non-ambient conditions, light-scattering particle size analysis, and field-emission scanning electron microscopy. As changing the amount of sodium can affect the conductivity of the material, efforts were made to keep the compositions of the final products as close as possible to the reaction conditions required to alter the crystal size. The zeolite samples were then exposed to different relative humidity (RH) conditions at various temperatures to observe how the formation of additional hydration layers on the surface of the material affects the conductivity. To gain insight into the interactions between zeolite and water, in terms of adsorption of lattice *versus* surface water, differential scanning calorimetry and thermogravimetric analysis were combined with impedance spectroscopy measurements.

Experimental

Materials

Chemicals used for the synthesis of faujasite (FAU) type zeolites were purchased from commercial sources: Ludox HS-30 (Sigma-Aldrich, 30.20% SiO_2, 69.66% H_2O, 0.14% Na_2O), sodium aluminate (Riedel de Haen, 42.40% Na_2O, 56.50% Al_2O_3, 1.10% H_2O), sodium hydroxide (Kemika, 76.70% Na_2O, 23.30% H_2O) and aluminium wire (Sigma-Aldrich, 99.99%).

Synthesis of microsized FAU zeolite (μ-FAU)

Ludox HS-30 (m = 10.20 g) was dissolved in a 33% aqueous solution of sodium hydroxide (m = 2.450 g). Sodium aluminate (m = 0.922 g) was dissolved in a mixture of 33% aqueous

solution of sodium hydroxide (m = 2.450 g) and water (m = 4.900 g). The reaction gel ($4Na_2O{\cdot}Al_2O_3{\cdot}10SiO_2{\cdot}158H_2O$) was obtained after the as-prepared sodium aluminate solution was slowly added to the well homogenized mixture of the silica source (Ludox solution), following the procedure described by Bosnar *et al.*[34] The gel was aged for 18 hours in a closed reaction vessel at room temperature. The vessel was then transferred to an oven at 100 °C for 48 hours, after which it was cooled to room temperature. The resulting μ-FAU product was washed until the rinse water reached a pH of 8, after which it was dried overnight at 60 °C.

Synthesis of nanosized FAU zeolite (n-FAU)

Ludox HS-30 (m = 30.00 g) was dissolved in a mixture of 33% aqueous solution of sodium hydroxide (m = 14.900 g) and water (m = 0.943 g). Aluminium wire (m = 0.592 g) was dissolved in a 33% water solution of sodium hydroxide (m = 15.210 g). The reaction gel ($8Na_2O{\cdot}0.7Al_2O_3{\cdot}10SiO_2{\cdot}160H_2O$) was obtained after the as-prepared aluminium-containing solution was added drop-wise to the well homogenized mixture of the silica source (Ludox solution), following the procedure described by Awala *et al.*[35] The gel was aged for 24 hours in a closed reaction vessel at room temperature. The vessel was then transferred to an oven at 120 °C for 70 minutes, after which it was cooled to room temperature. The resulting n-FAU product was washed until the rinse water reached a pH of 8, after which it was dried overnight at 60 °C.

Measurements

The powder X-ray diffraction (PXRD) data were collected in reflection mode with Cu Kα_1 radiation (λ = 1.54060 Å) on a Malvern Panalytical Empyrean diffractometer using a step size of 0.013° in a 2θ range between 4° and 70°. For non-ambient *in situ* PXRD measurements, a high-temperature camera (Anton Paar 1200N) was used in the temperature range of 25–400 °C and under vacuum conditions (p = 0.2 mbar). Analysis of the PXRD patterns was carried out using the TOPAS software (version 7.0).

Scanning electron microscopy imaging (SEM) and energy dispersive X-ray spectroscopy (EDX) were performed on a field emission scanning electron microscope (model JSM-7000F) operated at 10 keV. The particle size distribution analysis was carried out using a Malvern Mastersizer 2000 laser light-scattering particle (LLS) size analyser. Nitrogen physisorption was conducted using an Autosorb iQ3 (Quantachrome Instruments, Boynton Beach, FL, USA) at −196 °C. Prior to the measurement, the samples were degassed in vacuum at 250 °C for 10 h. The elemental composition of the samples was determined using flame atomic absorption spectrophotometer (AAS) PerkinElmer Analyst 200. Fourier-transformed infrared (FTIR) spectra were acquired using a PerkinElmer FTIR Frontier spectrometer, in the transmission mode under reduced pressure of 5×10^{-5} mbar and room temperature. The samples were activated beforehand by heating the self-supporting sample pastille at 400 °C for 3 hours under vacuum. Deuterated acetonitrile was used as a probe molecule and the amount of adsorbed acetonitrile was measured at 25 °C after saturation and subsequent evacuation.

Thermogravimetric analysis (TG) was carried out on a Shimadzu DTG-60H analyser at a rate of 10 °C min^{-1} from 25 °C to 500 °C under a flow of dry air. Differential scanning calorimetry (DSC) measurements were performed using a Netzsch DSC 214 Polyma calorimeter in the −20 °C to 450 °C range under the constant flow of pure nitrogen. The heating rate was 5 °C min^{-1}, and before measurements, the samples were exposed to either the desired RH atmosphere or dried at 140 °C for 24 hours before being transferred to aluminium crucibles and measured.

The electrical properties of materials were studied using an impedance analyser PalmSens4 from 10 Hz to 1 MHz in a hermetically closed chamber with a TEC-1091-NTC-PIN temperature controller. The relative humidity (RH) in the chamber was adjusted by exposure to ultrapure water (RH ∼ 100%) or to saturated aqueous solutions of NaBr (RH ∼ 60%) and NaCl (RH ∼ 75%). The samples were kept under these conditions for 24 hours prior to measurements. Measurements under vacuum were carried out after the sample was dried overnight at 140 °C and then transferred to the chamber evacuated to 100 mbar for 4 hours before measurements. For measurements, the polycrystalline sample was pressed into a cylindrical pellet (at around 2 tons of pressure) with a diameter of 5 mm and a thickness of 0.5 mm having 3.5 mm diameter sputter coated gold electrodes on the opposite surfaces of the pellet. The silver wires were then connected to gold electrodes using silver colloidal solution as glue. The impedance spectra were analysed by equivalent circuit modelling using a nonlinear least-squares fitting procedure in PSTrace software.

Results and discussion

Structural and microstructural characteristics

The PXRD patterns (Fig. S1) show that the peak positions of both μ-FAU and n-FAU correspond to those simulated from the crystal structure of the FAU-type zeolite.[36–38] The PXRD patterns were fitted in the space group $Fd\bar{3}m$ using the Pawley method, giving the values of unit cell parameters a = 24.6946 Å for μ-FAU and a = 24.9578 Å for n-FAU. The μ-FAU sample exhibits sharper Bragg peaks suggesting high crystallinity (Fig. 1a), while broadening of the peaks in the n-FAU diffraction pattern indicates smaller diffraction domains (Fig. 1b). The influence of the increased temperature and vacuum conditions on the FAU framework was investigated using non-ambient powder X-ray diffraction. As expected, both μ-FAU and n-FAU samples remain stable up to 400 °C, as shown by the minimal changes in their diffraction patterns (Fig. S2 and S3). The most noticeable difference between the PXRD patterns of μ-FAU collected at room temperature and at 400 °C (under reduced pressure) is the disappearance of the diffraction peak of the (222) plane, which passes through the centre of the hexagonal prism and is located at 12.38° 2θ in the hydrated sample, and the appearance of a new peak at 17.56° 2θ in the dehydrated sample, corresponding to the (422) plane, which passes through the sodalite cage. The subtle differences between the room temperature and non-ambient diffraction patterns of μ-FAU arise mainly from

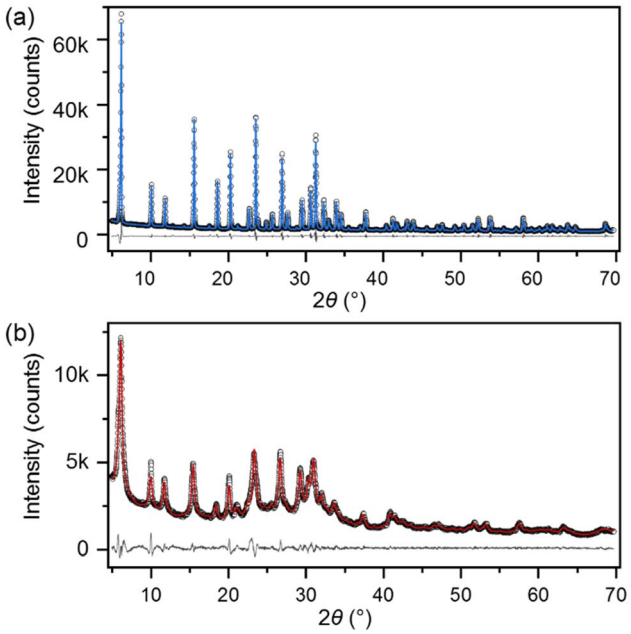

Fig. 1 Powder X-ray diffractograms showing experimental (black circles) and Pawley refinement (blue/red line), with the difference plot (grey line) for: (a) μ-FAU sample (R_{wp} = 6.9%) and (b) n-FAU sample (R_{wp} = 4.3%).

lattice expansion and the removal of water molecules, accompanied by the migration of sodium cations.[39]

With sufficient heating, all of the surface water and a majority of lattice water are desorbed and released from the zeolite. Therefore, sodium cations gain freedom to move and redistribute within the framework, as supported by the appearance of reflections indicating the presence of additional atoms inside the sodalite cage.[40,41]

The scanning electron microscope images (Fig. 2c and d) further confirm the size difference between the samples. The μ-FAU sample consists of 1–2 μm plate-like crystals (Fig. 2c), while the n-FAU sample consists of nanometre particles, whose geometry cannot be defined at the same magnification (20 000×). Particle size analysis by laser light scattering (Fig. 2a) shows relatively broad particle size distributions and indicates that the average particle size of both samples is larger than that of the individual crystallites due to agglomeration. Despite the agglomeration, the one order of magnitude particle size difference between n-FAU and μ-FAU observed in the SEM images is also reflected in the LLS measurements.

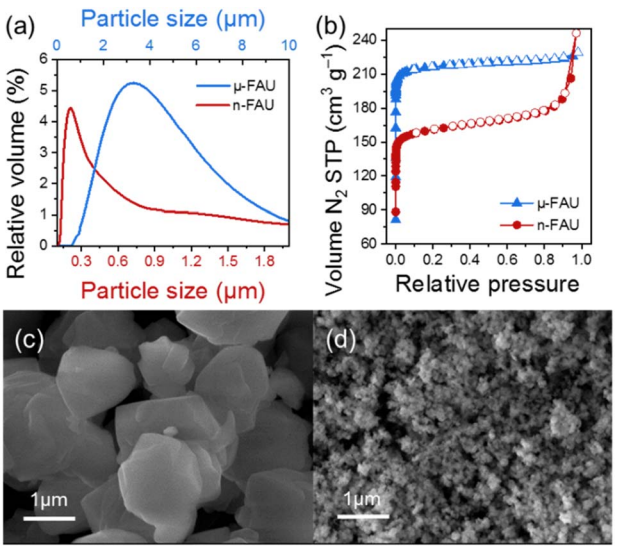

Fig. 2 Structural and microstructural analysis of prepared μ-FAU and n-FAU samples: (a) LLS particle size distribution; (b) N_2 porosimetry measurements; (c) SEM image of μ-FAU; (d) SEM image of n-FAU.

Porosity measurements of the μ-FAU sample exhibit a classic type I isotherm, with high nitrogen uptake at low pressures followed by a plateau at higher pressures, while n-FAU shows a combination of type I and type IV isotherms (Fig. 2b). The observed difference in nitrogen adsorption isotherms between n-FAU and μ-FAU samples arises from subtle differences in chemical composition and distinct sample morphologies. The n-FAU sample exhibits lower nitrogen adsorption uptake because its lower Si/Al ratio requires more sodium ions to balance the charge.[42] The increased sodium ion content in the n-FAU structure leads to a loss of micropore volume and consequently lower BET values. In contrast, μ-FAU has a higher pore volume and higher BET values than n-FAU (Table 1), which is attributed to its lower sodium content. This correlates with the different synthetic protocols used to prepare the targeted zeolites: n-FAU is prepared in a shorter time and at a higher temperature than μ-FAU, resulting in a greater number of structural defects. After oven drying, these defects cause n-FAU to agglomerate more readily, as supported by LLS data and porosimetry measurements at high pressure.[43] This behaviour in nanosized samples was previously observed by Awala *et al.* in FAU-type zeolites.[35] The consequences of agglomeration are also reflected in the outer surface area, which is lower than expected for the n-FAU sample.

Spectroscopic characterization

The textural properties of the samples were further analysed using Fourier transform infrared spectroscopy in a vacuum. In the higher frequency range of the spectra of both samples, three different types of bands associated with the hydroxyl groups can be recognized (Fig. 3a). The band at 3745 cm^{-1} is assigned to the isolated ν(Si–OH) stretching vibration.[10] The sharp band with high intensity at 3690 cm^{-1} is generally assumed to be related to the interactions of the terminal –OH groups with the sodium cation.[44] Several broad bands in the 3600–3000 cm^{-1} range indicate the presence of structural defects in the samples, namely silanol "nests"; parts of the structure rich in silanol groups whose hydrogen bonds cause a band shift to lower wavenumbers compared to the isolated Si–OH.[26] All the aforementioned bands are of higher intensity in n-FAU, which is to be expected as they mostly originate from vibrations associated with surface defects. In both spectra there are no visible bands at 3480 and 3660 cm^{-1} from extra-framework aluminium species.[45] To further confirm this, the acidity of the sample was analysed using D_3-acetonitrile as a probe molecule (Fig. 3b), and only very weak Si–OH Lewis acid sites at ~2272 cm^{-1} are present

Table 1 Sample composition and textural properties of n-FAU and μ-FAU

Sample	Composition	Si/Al	Na/Al	BET/$m^2\ g^{-1}$	$S_{external}/m^2\ g^{-1}$
μ-FAU	$0.18Na_2O : 0.19Al_2O_3 : SiO_2$	2.63	0.95	894	32.6
n-FAU	$0.29Na_2O : 0.3Al_2O_3 : SiO_2$	1.66	0.97	649	60.5

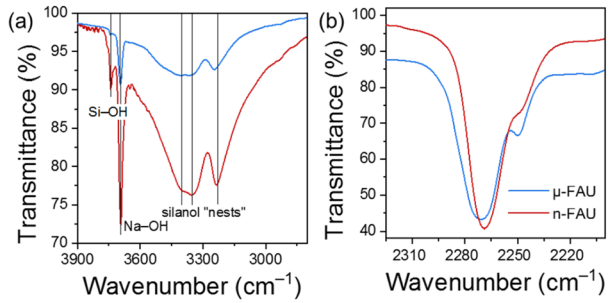

Fig. 3 Spectroscopic characterization of μ-FAU and n-FAU samples: (a) vacuum FTIR spectra of the samples in the higher frequency region; (b) D_3-acetonitrile adsorbed on the samples at 25 °C.

in both samples.[46] This type of spectra is expected for the FAU-type zeolite sample that contains only sodium as counterions. The band at 2327 cm^{-1}, which would originate from D_3-acetonitrile bound to hexacoordinated Al^{3+} species (aluminium outside the framework), is absent from both spectra, and no other bands appear that would indicate binding of the probe molecules to Brønsted acid sites (protonated Si–O–Al bridges). This demonstrates that there are no other charge-balancing cations in the framework that could later complicate the interpretation of the results.[46]

Thermal stability

Thermogravimetric analysis and differential scanning calorimetry were performed on differently conditioned n-FAU and μ-FAU zeolite samples to distinguish the interactions between water within the zeolite framework and on the surface. Thermogravimetric analysis of fully hydrated samples (samples conditioned at 100% RH) shows that two distinct steps of water removal can be identified for both n-FAU and μ-FAU zeolites (Fig. S4). The first step corresponds to the release of moderately bound water on the surface (extrinsic water), while intrinsic water leaves the zeolite lattice at significantly higher temperatures. Mass loss associated with these steps, as shown in Table 2, indicates that the amount of water contained in the lattice is equal for both zeolite samples, while the amount of surface water in n-FAU is three times higher than in the μ-FAU sample. The external surface area (Table 1) of n-FAU is twice that of μ-FAU, which explains the significantly higher amount of surface water in n-FAU.

Table 2 Thermal analysis of μ-FAU and n-FAU samples: mass loss and enthalpies related to dehydration calculated from the thermogravimetric analysis and differential scanning calorimetry, respectively

	$w(H_2O,$ RH = 100%)/%			
Sample	Surface	Lattice	ΔH_{dry}/kJ mol^{-1}	ΔH_{100}/kJ mol^{-1}
μ-FAU	5.74	22.2	358.3	807.4
n-FAU	19.49	23.0	453.3	866.3

This difference in the amount of extrinsic water is clearly evident in the DSC measurements (Fig. 4). In both n-FAU and μ-FAU samples, complete water elimination occurs at 450 °C. For n-FAU and μ-FAU samples dried at 140 °C prior to DSC measurements, the remaining water is eliminated more rapidly in the n-FAU sample due to the shorter diffusion path and the presence of macropores in the agglomerates. The deviation for the baselines of different curves of the same sample is caused by the change in heat capacity (ΔC_p) between the hydrated and dried phases. DSC analysis enables the clearer distinction of processes associated with water loss; for example, two additional peaks are observed for both samples at temperatures below 110 °C. The most intense peak at 108 °C for n-FAU and 87 °C for μ-FAU could be associated with the evaporation of water molecules that form hydrogen bonds and coat the surface of the zeolite samples. The behaviour of these water molecules is more similar to that of free liquid water, which is why they are referred to as "liquid-like" water layers. However, the n-FAU and μ-FAU samples, having hydroxyl-rich surfaces, are also able to form strong hydrogen bonds with additional water molecules. These molecules tend to arrange in more structured layers and are called "ice-like" water layers.[24,26] When comparing the DSC peaks around 100 °C after deconvolution, it can be seen that the enthalpy of water removal for the μ-FAU sample (ΔH = 103.5 kJ mol^{-1}) is more than three times lower than that of n-FAU (ΔH = 339.8 kJ mol^{-1}), indicating weaker interactions between surface water and the sample. The main reason for this could be the lower number of silanol "nests" in μ-FAU, which are known to form strong hydrogen bonds with water molecules.[10,26] However, strong interactions of "ice-like" water with the surface make it difficult to distinguish the elimination of surface water from the removal of lattice water from the

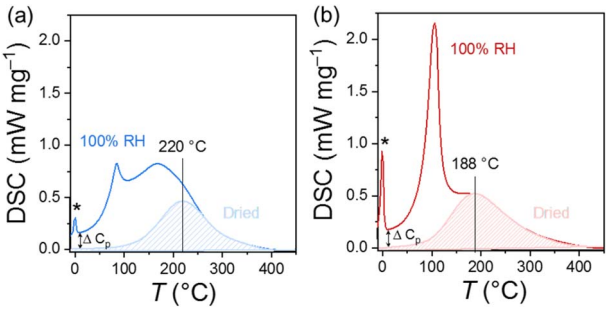

Fig. 4 DSC curves of the hydrated and dried (at 140 °C) (a) μ-FAU and (b) n-FAU samples measured at a heating rate of 5 °C min^{-1}.

channels. The DSC endotherm peak at 0 °C (labelled with an asterisk in Fig. 4) originates from the melting of the hydration layers, which turned to ice after the sample was cooled to −20 °C. This behaviour was observed in earlier studies of zeolites, where the reported melting peak was attributed to the heterogeneous nucleation of water molecules, which correlates well with our observations of a "liquid-like" water layer.[47]

Electrical characterization

The preparation of two chemically and structurally analogous FAU zeolites with a significant difference in particle size enabled investigation of the extent to which microstructure is important for the electrical properties. Both n-FAU and μ-FAU compressed zeolite pellets used for measurement were prepared and treated identically to ensure a direct correlation between microstructure and ionic conductivity. Impedance spectroscopy measurements were carried out at various humidity levels (RH = 60%, 75%, 100%) and under dry conditions achieved by reducing the pressure to 100 mbar, which allowed the crucial impact of water from ambient air on the overall electrical performance to be accounted for. Prior to measurements at reduced pressure, the samples were pre-treated overnight at 140 °C to remove excess water. The aim was to remove only the water adsorbed on the surface, while leaving the more tightly bound lattice water in place. In this context, the term "dry" in Fig. 5 indicates that the samples of n-FAU and μ-FAU are free of extrinsic water but contain intrinsic lattice water. Complex impedance plane diagrams of n-FAU and μ-FAU samples (Fig. 5) measured under two boundary conditions, under vacuum and at RH 100%, show that the removal of water molecules from the surface reduces the conductivity by at least three orders of magnitude. This indicates that the charge transfer in FAU zeolites is strongly facilitated by water molecules adsorbed on the surface. The difference in conductivity is even more pronounced in n-FAU samples under dry and humid conditions. Graphical representations of the complex impedance plane for n-FAU and μ-FAU samples at 100% RH show different ratios between the contributions of the intrinsic lattice (bulk, B) and the extrinsic surface (grain boundary, GB) to the conductivity. Thus, the complex impedance spectrum can be described by two parallel (resistor-constant phase element) equivalent circuits connected in series, where the semicircle at higher frequencies represents the crystal or bulk, and the semicircle at lower frequencies is associated with the grain boundaries, resulting from the polycrystalline form of the pressed pellet used for measurements.[25] For the dry μ-FAU sample under vacuum conditions, the contribution of the crystal bulk to the conductivity is $\sigma_B = 1.97 \times 10^{-5}$ S cm^{-1}, a value two orders of magnitude higher than that of the grain boundary, $\sigma_{GB} = 5.29 \times 10^{-7}$ S cm^{-1}. In contrast, σ_B in n-FAU remains higher than σ_{GB}, but the ratio between the two is less skewed towards bulk conductivity ($\sigma_B = 3.00 \times 10^{-7}$ S cm^{-1} and $\sigma_{GB} = 0.879 \times 10^{-7}$ S cm^{-1}, respectively). The higher overall conductivity of dry μ-FAU is expected, as continuous channels and formed water clusters in larger zeolite particles provide abundant proton-conducting sites,[16] enabling more efficient charge transfer. The spectra recorded after the sample was stored for 24 hours in an atmosphere with 100% RH clearly show the pronounced effect of water molecules on conductivity. The conductivity of n-FAU increases sharply ($\sigma = 2.75 \times 10^{-3}$ S cm^{-1}), making it impossible to distinguish individual contributions from the bulk and grain boundary. In contrast, two distinct semicircles can be observed in the complex impedance plane graph of the μ-FAU sample. Surprisingly, in this case, the bulk conductivity has a lower σ value ($\sigma_B = 6.27 \times 10^{-4}$ S cm^{-1}) than the grain boundary conductivity ($\sigma_{GB} = 3.25 \times 10^{-3}$ S cm^{-1}). This indicates that the water content within the lattice of a zeolite crystallite contributes less to the overall conductivity than the water layers adsorbed on the surface of the zeolite.

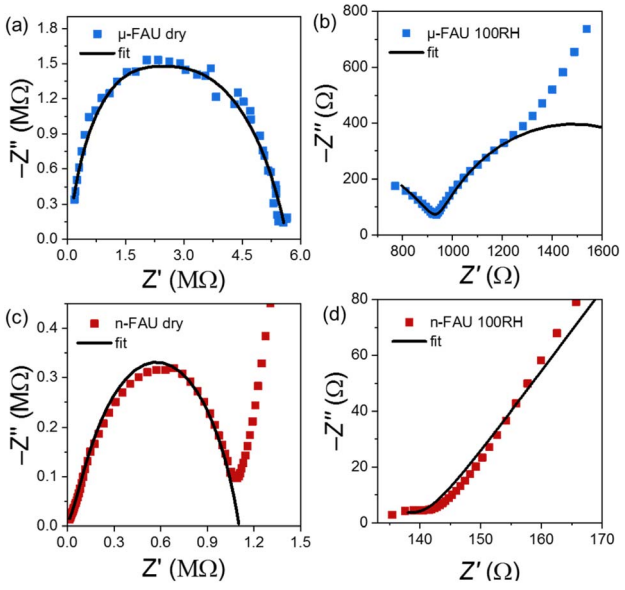

Fig. 5 Complex impedance plane graph measured at 25 °C for samples: (a) dried μ-FAU at reduced pressure; (b) hydrated μ-FAU at 100% RH and ambient pressure; (c) dried n-FAU at reduced pressure; (d) hydrated n-FAU at 100% RH and ambient pressure.

The effect of relative humidity on the proton conductivities at different temperatures for both samples is shown in Fig. 6 and in the SI (Fig. S5 and S6). The Arrhenius plot of the μ-FAU sample (Fig. 6a) at 60% RH shows a linear increase across the entire temperature range (from 5 to 60 °C), from which the activation energy, E_a, of 54 kJ mol^{-1} is calculated. A further increase in RH leads to a disruption of this trend, as the behaviour at 75% and 100% RH is linear only up to 20 °C, after which the conductivity decreases rapidly. This decrease is associated with thermally assisted surface water removal, which is observed in the TG (Fig. S4) and DSC curves (Fig. 4) as well. In addition, a further increase in temperature to 60 °C results in the conductivity values for different humidities finally converging. This indicates that at high humidity, the main contribution to the overall conductivity comes from the conductivity of the hydration water layers. Therefore, the activation energies, 71 kJ mol^{-1} (75% RH) and 80 kJ mol^{-1} (100% RH), were calculated from data collected in the lower temperature range. Regardless of the trend change caused by

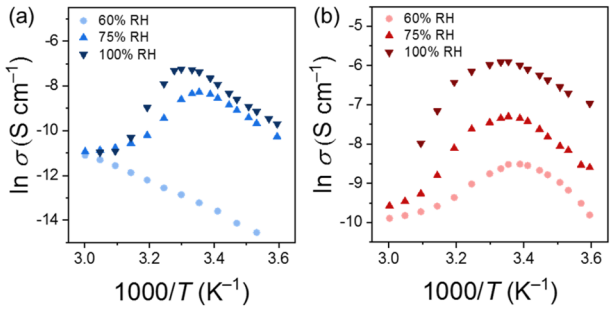

Fig. 6 Arrhenius plot of proton conductivity of (a) μ-FAU and (b) n-FAU samples measured at different relative humidity levels.

dehydration, the E_a values for all investigated humidity levels in the μ-FAU sample indicate a vehicle mechanism for proton transport. On the other hand, the Arrhenius diagrams of the n-FAU samples (Fig. 6b) show the same trend of increasing conductivity at lower temperatures and decreasing above 20 °C. The only difference is that the conductivity drops more sharply above 20 °C as the RH increases. At 60% RH, the activation energy of the n-FAU sample is similar ($E_a = 56$ kJ mol^{-1}) to that of the μ-FAU sample at the same humidity. However, an increase in the water content on the sample surface achieved by exposing the zeolite to RH 75 and 100% leads to a decrease in activation energy to 53 kJ mol^{-1} and 37 kJ mol^{-1}, respectively. This suggests that less tightly bound surface "liquid-like" water layers shift the proton conductivity towards the Grotthuss mechanism with lower energy (E_a < 38 kJ mol^{-1}).[30] The hydration threshold that triggers the significant transition from vehicular to proton hopping conduction in n-FAU is above 75% RH (Fig. 7). The nanosized morphology of n-FAU enables this transition efficiently due to a higher number of surface defects, isolated Si–OH groups, and silanol "nests". Silanol nests form very strong interactions with water molecules, allowing the formation of more strongly bound hydration water layers. Furthermore, theoretical calculations indicate that isolated Si–OH groups can have a pK_a of around 5, meaning that n-FAU can generate more protons to further promote proton hopping.[20]

The increase in activation energy of the μ-FAU sample with rising water content can be attributed to the displacement of the sodium cations. At higher water contents and Si/Al ratios above 2, the sodium cation moves from the hexagonal prism (Fig. 7b), where it is coordinated with six framework oxygen atoms, to the entrance of the sodalite cage.[48,49] Once this shift occurs, the sodium cation can coordinate water molecules within the sodalite cage, increasing the residence time of water molecules within the channels and leading to a decrease in the diffusion rate.[10] This interaction, already present in n-FAU due to its high Si/Al ratio, disrupts the formation of water molecule clusters that tend to promote diffusion.[12,13] For that reason, the less favourable diffusion through channels is completely bypassed by the conductivity at the grain boundaries and surfaces.

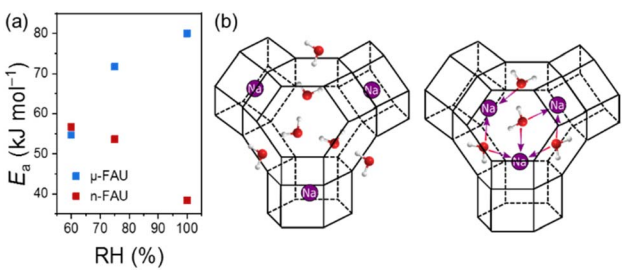

Fig. 7 (a) Dependence of proton conductivity activation energy (E_a) of μ-FAU and n-FAU samples on the relative humidity; (b) schematic of sodium cation migration in the FAU zeolite framework at increased water loadings.

Conclusions

The proton conductivity of faujasite Na-FAU type zeolites with different particle sizes was measured at various relative humidity levels to distinguish the contributions of intrinsic (lattice) and extrinsic (surface) water to overall conductivity. Compared to the microsized μ-FAU sample, the nanosized particle sample, n-FAU, absorbed more extrinsic water because its surface is rich in structural defects (silanol "nests"), which are better suited to generate stronger hydrogen-bonding interactions. A decrease in particle size had a significant impact on conductivity under all measurement conditions, with the difference becoming even more pronounced at higher humidity (ranging from several times higher under low humidity and low pressure conditions to several orders of magnitude higher at 100% RH). Furthermore, increasing humidity caused a change in the conductivity mechanism of the samples, with the "liquid-like" water layer-rich n-FAU sample shifting more heavily towards the lower energy Grotthuss mechanism, while the activation energy for proton transfer in the μ-FAU sample continued to increase (vehicular mechanism). This indicates that, regardless of humidity, the μ-FAU sample cannot form hydration layers as thick as those of n-FAU, and most proton conductivity occurs within the zeolite channels. An increase in lattice water content in FAU-type zeolite causes the framework sodium atoms to shift towards the sodalite cage, which decreases the diffusion rate and directly increases the proton transfer activation energy. Overall, these studies show that zeolites hold great potential for effective construction and regulation of proton transport through their intrinsic channels and extrinsic large surface area, offering tuneable performance in proton conductivity as well as chemical and structural stability, durability, and sustainability. One way to achieve high conductivity in zeolites is to stabilise a greater amount of "liquid-like" surface water through encapsulation or low-temperature manipulation. The functionalisation of the zeolite surface with Brønsted acid sites, which can be deprotonated more readily than silanols and theoretically boost surface conductivity, is a second strategy that could lead to a less structured state.

Conflicts of interest

There are no conflicts to declare.

Data availability

The data supporting this article are given in the supplementary information (SI). Supplementary information: PXRD analysis (Fig. S1–S3), TG/DTA (Fig. S4), impedance spectroscopy data (Fig. S5 and S6). See DOI: https://doi.org/10.1039/d5ta10130a.

Acknowledgements

G. M. S. acknowledges support from the internal RBI funding scheme MZ-2025 program (MZ3-25) through the National Recovery and Resilience Plan 2021–2026 (NPOO), funded by the European Union's NextGenerationEU program. J. M. acknowledges the financial support of the Slovenian Research and Innovation Agency through the research program Nanoporous Materials (P1-0021).

Notes and references

1 L. I. Rodionova, E. E. Knyazeva, S. V. Konnov and I. I. Ivanova, *Pet. Chem.*, 2019, **59**, 455–470.
2 R. Wei, X. Liu, L. Cao, C. Chen, I. C. Chen, Z. Li, J. Miao and Z. Lai, *Nat. Commun.*, 2024, **15**, 1–11.
3 M. Salimian, O. Okhay, R. Krishna, E. Titus, J. Gracio, L. Guerra, J. Ventura, C. Freire, C. Pereira, P. R. Babu and R. S. Khairnar, *Polym. Int.*, 2013, **62**, 1583–1588.
4 M. Álvaro, J. F. Cabeza, D. Fabuel, H. García, E. Guijarro and J. L. M. de Juan, *Chem. Mater.*, 2006, **18**, 26–33.
5 H. Shi, J. Zhang and J. Li, *RSC Adv.*, 2021, **11**, 5393–5398.
6 T. Wang, Y. Chu, X. Li, Y. Liu, H. Luo, D. Zhou, F. Deng, X. Song, G. Lu and J. Yu, *J. Am. Chem. Soc.*, 2023, **145**, 5342–5352.
7 M. S. Dickson, S. G. Shumway, G. Neilsen, A. Navrotsky and B. F. Woodfield, *J. Chem. Thermodyn.*, 2023, **181**, 107023.
8 B. Hunger, S. Matysik, M. Heuchel, E. Geidel and H. Toufar, *J. Therm. Anal.*, 1997, **49**, 553–565.
9 A. Di Lella, N. Desbiens, A. Boutin, I. Demachy, P. Ungerer, J. P. Bellat and A. H. Fuchs, *Phys. Chem. Chem. Phys.*, 2006, **8**, 5396–5406.
10 E. A. Paukshtis, M. A. Yaranova, I. S. Batueva and B. S. Bal'zhinimaev, *Microporous Mesoporous Mater.*, 2019, **288**, 109582.
11 A. J. Porter and A. J. O'Malley, *J. Phys. Chem. C*, 2021, **125**, 11567–11579.
12 C. J. Heard, L. Grajciar, F. Uhlík, M. Shamzhy, M. Opanasenko, J. Čejka and P. Nachtigall, *Adv. Mater.*, 2020, **32**, 2003264.
13 A. Özgür Yazaydın and R. W. Thompson, *Microporous Mesoporous Mater.*, 2009, **123**, 169–176.
14 J. Hunger, I. A. Beta, H. Böhlig, C. Ling, H. Jobic and B. Hunger, *J. Phys. Chem. B*, 2006, **110**, 342–353.
15 M. Ivanova, E. Dib, S. Mintova, E. B. Clatworthy and L. Grunin, *Langmuir*, 2026, **42**, 3647–3655.
16 J. H. Hack, J. P. Dombrowski, X. Ma, Y. Chen, N. H. C. Lewis, W. B. Carpenter, C. Li, G. A. Voth, H. H. Kung and A. Tokmako, *J. Am. Chem. Soc.*, 2021, **143**, 10203–10213.
17 H. Windeck, D. Willimetz, A. Erlebach, C. J. Heard, F. Berger and J. Sauer, *J. Phys. Chem. Lett.*, 2026, **17**, 1201–1206.
18 W. J. Roth, B. Gil, K. A. Tarach and K. Góra-Marek, *Chem. Soc. Rev.*, 2025, **54**, 7484–7560.
19 P. Lu, J. Xu, Y. Sun, R. Guillet-Nicolas, T. Willhammar, Z. Liu, H. Yu, X. Yang, Q. Lang, S. Mintova and X. Zou, *Nature*, 2024, **636**, 368–373.
20 M. Sulpizi, M.-P. Gaugeot and M. Sprik, *J. Chem. Theory Comput.*, 2012, **8**, 1037–1047.
21 T. Defferriere, D. Klotz, J. C. Gonzalez-Rosillo, J. L. M. Rupp and H. L. Tuller, *Nat. Mater.*, 2022, **21**, 438–444.
22 E. Celik, Y. Ma, T. Brezesinski and M. T. Elm, *Phys. Chem. Chem. Phys.*, 2021, **23**, 10706–10735.
23 X. Sun, E. Vøllestad, P. M. Rørvik, S. Prodinger, G. N. Kalantzopoulos, A. Chatzitakis and T. Norby, *Appl. Surf. Sci.*, 2023, **611**, 1–12.
24 S. Ø. Stub, E. Vøllestad and T. Norby, *J. Phys. Chem. C*, 2017, **121**, 12817–12825.
25 S. Stub, E. Vøllestad and T. Norby, *J. Mater. Chem. A*, 2018, **6**, 8265–8270.
26 D. B. Asay and S. H. Kim, *J. Phys. Chem. B*, 2005, **109**, 16760–16763.
27 A. Afonja, R. Binions, S. Dungey, I. P. Parkin, D. W. Lewis and D. E. Williams, *Procedia Eng.*, 2010, **5**, 103–106.
28 O. Schäf, H. Ghobarkar and U. Guth, *Ionics*, 1999, **5**, 1–7.
29 D. W. Lim and H. Kitagawa, *Chem. Rev.*, 2020, **120**, 8416–8467.
30 S. Wang, M. Wahiduzzaman, L. Davis, A. Tissot, W. Shepard, J. Marrot, C. Martineau-Corcos, D. Hamdane, G. Maurin, S. Devautour-Vinot and C. Serre, *Nat. Commun.*, 2018, **9**, 1–8.
31 M. Dunatov, K. Molčanov, Z. Štefanić, R. Kruk and L. Androš Dubraja, *Inorg. Chem.*, 2024, **63**, 163–172.
32 O. Schäf, H. Ghobarkar and U. Guth, *Ionics*, 1997, **3**, 282–288.
33 P. Choeichom and A. Sirivat, *Ionics*, 2018, **24**, 2829–2841.
34 S. Bosnar, D. Bosnar, N. Ren, N. Rajić, B. Gržeta and B. Subotić, *J. Porous Mater.*, 2013, **20**, 1329–1336.
35 H. Awala, J. Gilson, R. Retoux, P. Boullay, J. Goupil, V. Valtchev and S. Mintova, *Nat. Mater.*, 2015, **14**, 1–5.
36 https://europe.iza-structure.org/IZA-SC/framework.php?ID=93, accessed october 2025.
37 D. H. Olson, *J. Phys. Chem.*, 1970, **74**, 2758–2764.
38 D. H. Olson, *Zeolites*, 1995, **15**, 439–443.
39 J. J. Van Dun, K. Dhaeze and W. J. Mortier, *J. Phys. Chem.*, 1988, **92**, 6747–6754.
40 C. A. C. Perez, N. S. de Resende, V. M. M. Salim and M. Schmal, *J. Phys. Chem. C*, 2017, **121**, 2755–2761.
41 C. J. Gilmore, J. A. Kaduk and H. Schenk, *International Tables for Crystallography, Volume H, Powder Diffraction*, Wiley, 1st edn, 2019, vol. H.
42 A. Osatiashtiani, B. Puértolas, C. C. S. Oliveira, J. C. Manayil, B. Barbero, M. Isaacs, C. Michailof, E. Heracleous, J. Pérez-Ramírez, A. F. Lee and K. Wilson, *Biomass Convers. Biorefinery*, 2017, **7**, 331–342.
43 L. H. Chen, S. T. Xu, X. Y. Li, G. Tian, Y. Li, J. C. Rooke, G. S. Zhu, S. L. Qiu, Y. X. Wei, X. Y. Yang, Z. M. Liu and B. L. Su, *J. Colloid Interface Sci.*, 2012, **377**, 368–374.

44 T. M. Salama, T. Shido, H. Minagawa and M. Ichikawa, *J. Catal.*, 1995, **152**, 322–330.
45 M. Niwa, S. Nishikawa and N. Katada, *Microporous Mesoporous Mater.*, 2005, **82**, 105–112.
46 K. Hadjiivanov, *Identification and Characterization of Surface Hydroxyl Groups by Infrared Spectroscopy*, Elsevier Inc., 1st edn, 2014, vol. 57.
47 A. H. Janssen, H. Talsma, M. J. van Steenbergen and K. P. de Jong, *Langmuir*, 2004, **20**, 41–45.
48 C. Beauvais, A. Boutin and A. H. Fuchs, *C. R. Chim.*, 2005, **8**, 485–490.
49 C. Abrioux, B. Coasne, G. Maurin, F. Henn, M. Jeffroy and A. Boutin, *J. Phys. Chem. C*, 2009, **113**, 10696–10705.